Confinement-driven electronic and topological phases in corundum-derived 3*d*-oxide honeycomb lattices

Okan Köksal, Santu Baidya, and Rossitza Pentcheva*

Department of Physics and Center for Nanointegration Duisburg-Essen, University of Duisburg-Essen, Lotharstrasse 1, 47057 Duisburg, Germany

(Received 30 March 2017; published 12 January 2018)

Using density functional theory calculations including an on-site Coulomb term, we explore electronic and possibly topologically nontrivial phases in 3*d* transition-metal oxide honeycomb layers confined in the corundum structure (α-Al_2O_3) along the [0001] direction. In most cases the ground state is a trivial antiferromagnetic Mott insulator, often with distinct orbital or spin states compared to the bulk phases. With imposed symmetry of the two sublattices the ferromagnetic phases of $(X_2O_3)_1/(Al_2O_3)_5(0001)$ with X = Ti, Mn, Co, and Ni exhibit a characteristic set of four bands, two that are relatively flat and two with a Dirac crossing at K, associated with the single-electron occupation of e'_g (Ti) or e_g (Mn, Co, Ni) orbitals. Our results indicate that the Dirac point can be tuned to the Fermi level using strain. Applying spin-orbit coupling (SOC) leads to a substantial anomalous Hall conductivity with values up to 0.94 e^2/h. Moreover, at $a_{Al_2O_3} = 4.81$ Å we identify a particularly strong effect of SOC with an out-of-plane easy axis for $(Ti_2O_3)_1/(Al_2O_3)_5(0001)$ which stabilizes the system dynamically. Due to the unusually high orbital moment of $-0.88\mu_B$ that nearly compensates the spin moment of $1.01\mu_B$, this system emerges as a candidate for the realization of the topological Haldane model of spinless fermions. Parallels to the perovskite analogs $(LaXO_3)_2/(LaAlO_3)_4(111)$ are discussed.

DOI: 10.1103/PhysRevB.97.035126

I. INTRODUCTION

Progress in growth techniques like molecular beam epitaxy and pulsed laser deposition has enabled the growth of transition-metal oxide (TMO) superlattices with atomic precision. This has opened possibilities to explore emergent phenomena and electronic as well as magnetic phases in reduced dimensions that are not available in the parent compounds [1–4]. Beyond the [001] growth direction, where confinement can lead to a metal-to-insulator transition, e.g., in $LaNiO_3/LaAlO_3(001)$ superlattices (SLs) [5–7], in (111)-oriented perovskite superlattices a buckled honeycomb lattice is formed by each two X-cation triangular lattices of the AXO_3 perovskite structure, as suggested by Xiao *et al.* [8]. As early as 1988 Haldane [9] predicted a quantized Hall conductance arising from spinless fermions on a honeycomb lattice in the absence of an external magnetic field. This model serves as a prototype of the quantum anomalous Hall insulators (QAHI) that are of interest for future applications in low-power electronics devices or in the search of Majorana fermions [10,11]. Material realizations of QAHIs are being sought in Mn-doped HgTe or Cr- and Fe-doped Bi_2Te_3, Bi_2Se_3, and Sb_2Te_3 [12–14], in 5*d* transition metals on graphene [15,16], or in TMO with rocksalt- (EuO/CdO [17] and EuO/GdO [18]) or rutile-derived heterostructures [19–21] or double perovskites [22,23]. While the relevant orbitals in common topological insulators are *s* and *p*, the correlated nature of the *d* electrons in transition-metal oxides suggests a richer functional behavior.

In this context, the initial proposal of Xiao *et al.* [8] offered a fertile playground to explore the realization of topologically nontrivial phases in perovskite superlattices with a honeycomb pattern [24–33]. A recent systematic density functional theory (DFT) + U study of the 3*d* series in $(LaXO_3)_2/(LaAlO_3)_4(111)$ superlattices [34] revealed a broad set of competing charge, magnetic, and orbitally ordered phases. Among the 3*d* series, the $LaMnO_3$ buckled honeycomb bilayer represents a promising candidate with a topological transition from a high-symmetry Chern insulator with a substantial gap (150 meV) to a Jahn-Teller distorted trivial Mott insulating ground state. The insight obtained in this study, especially on the effect of band filling and strain, has served to identify robust Chern insulators in the 4*d* and 5*d* series (e.g., $LaOsO_3$ and $LaRuO_3$ bilayers) [35].

Besides the (111)-oriented perovskite SLs, a honeycomb lattice can also be found in other structure types, such as the corundum structure, as mentioned in [8], where each metal ion bilayer forms a honeycomb pattern with a much lower degree of buckling than in the perovskite case. Another qualitative difference is the type of connectivity in the structure. While in the perovskite only corner connectivity is present, in the corundum the XO_6 octahedra are edge sharing in plane and alternating corner and face sharing out of plane (see Fig. 1). This difference in connectivity implies different interaction mechanisms between neighboring sites with a potential impact on the electronic and magnetic behavior compared to the perovskite superlattices. Therefore, we perform here a systematic study of the ground-state properties of 3*d* honeycomb layers incorporated in the band insulator Al_2O_3, as shown in Fig. 1, and compare those to the perovskite analogs [34]. Recently, Afonso and Pardo [36] addressed the possibility of topological phases in 5*d* honeycomb layers sandwiched in the corundum structure, concentrating primarily on cases that preserve time-reversal and inversion symmetry. In contrast,

*Rossitza.pentcheva@uni-due.de

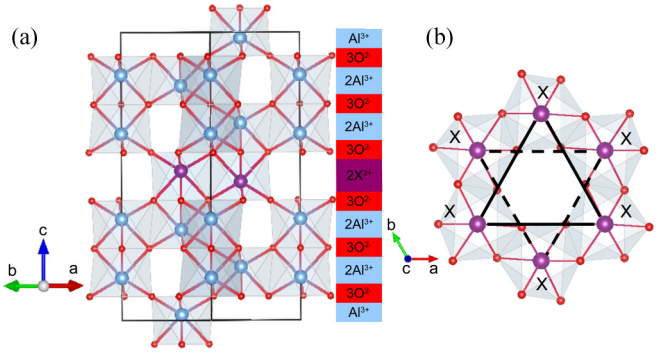

FIG. 1. (a) Side view of the $(X_2O_3)_1/(Al_2O_3)_5(0001)$ superlattice where one metal ion bilayer in the corundum structure is exchanged with a $X = 3d$ ion. (b) Top view of the buckled honeycomb lattice in the a-b plane; solid and dashed lines connect the next-nearest TM-ion neighbors residing on the two sublattices.

in the $3d$ cases the electronic correlations are much more pronounced, leading to a stronger affinity for magnetically ordered states. Here we take into account the possibility of time-reversal symmetry breaking, resulting in a variety of competing magnetic and electronic phases. Analogous to the [111]-oriented perovskite heterostructures [34], there is no polar mismatch at the interface between X_2O_3 and Al_2O_3, and both the X and Al ions are formally in the 3+ oxidation state (except for the disproportionation found in the case of $X =$ Ni that will be discussed below). We also compare the properties of the SLs to the bulk parent compounds (see more information in the Supplemental Material [37]).

The remainder of this paper is structured as follows: In Sec. II we give a brief description of the computational details and studied systems; in Sec. III we discuss the ground and metastable states within the $3d$ series. In Sec. IV we investigate how the electronic properties can be tuned by strain. In Sec. V we analyze the effect of spin-orbit coupling (SOC) and the resulting anomalous Hall conductivity and Berry curvatures. Moreover, we identify a case of unusually strong spin-orbit effect. Finally, the results are summarized in Sec. VI.

II. THEORETICAL METHOD AND DETAILS

Density functional calculations were carried out for $(X_2O_3)_1/(Al_2O_3)_5(0001)$, $X = 3d$ ion, with the VASP [38] code using the projector augmented wave method [39]. For the exchange-correlation functional we applied the generalized gradient approximation (GGA) of Perdew, Burke, and Ernzerhof [40] and in some cases, for comparison, the local-density approximation (LDA) [37]. An on-site Coulomb repulsion parameter was considered within the GGA+U approach with $U = 5$ eV and Hund's exchange parameter of $J = 0.7$ eV on all TM ions X. We used the approach of Dudarev *et al.* [41], which considers $U_{\text{eff}} = U - J$. We have verified that the results are robust with respect to a reasonable variation of U and that LDA+U and GGA+U give qualitatively similar behaviors; further information is provided in the Supplemental Material [37]. Previous studies have shown that taking into account electronic correlations may result in a trivial antiferromagnetic (AFM) insulator for $5d$ systems, initially proposed as candidates for Z_2 TIs within tight-binding and DFT (GGA/LDA) studies. While for a $SrIrO_3$ honeycomb bilayer both DFT + dynamical mean-field theory (DMFT) [31] and DFT+U [28] show such a tendency, the effect of static vs dynamic correlations needs to be addressed in more detail in future studies.

The k-point mesh contains at least $6 \times 6 \times 2$ k points, including the Γ point; in some cases $9 \times 9 \times 3$ k points were used. A cutoff energy of 600 eV was chosen for the plane waves. Atomic positions were relaxed until the Hellman-Feynman forces were lower than 1 meV/Å. In selected cases, especially in order to explore high-symmetry metastable and symmetry-broken states, calculations were performed using the all-electron full-potential linearized augmented plane-wave method as implemented in the WIEN2K code [42]. The anomalous Hall conductivity (AHC) for potentially interesting cases is computed on a very dense k-point mesh of $300 \times 300 \times 50$ using the WANNIER90 code [43,44].

To model the $(X_2O_3)_1/(Al_2O_3)_5(0001)$ superlattices, an Al bilayer in the corundum structure is substituted by a $X = 3d$ bilayer (see Fig. 1). Systems grown on $Al_2O_3(0001)$ are simulated by fixing the lateral lattice constant to the GGA value of Al_2O_3. The lattice parameters of Al_2O_3 within GGA are $a = 4.81$ Å, $c = 13.12$ Å, approximately 1% larger than the experimental values $a = 4.76$ Å and $c = 12.99$ Å [45]. The internal parameters and the out-of-plane lattice parameter c were optimized for each system within GGA+U, and the results are given in Table II in the Supplemental Material [37]. Additionally, we calculated the structural and electronic properties of bulk X_2O_3, displayed in Table I in the Supplemental Material [37] together with previous experimental and theoretical results [46–62]. The lateral strain is defined as $\sigma(\%) = \frac{\Delta a}{a_{X_2O_3}}$, where $\Delta a = a_{Al_2O_3} - a_{X_2O_3}$ is the difference between the lateral lattice parameters of Al_2O_3 and bulk X_2O_3. We have considered both ferromagnetic (FM) and AFM coupling and performed the relaxations for each spin arrangement for both the bulk compounds and the SLs. As mentioned above, the degree of buckling is much lower for the corundum-derived honeycomb layers (0.39–0.63 Å; see Table II in the Supplemental Material [37]) compared to the perovskite analogs (2.27–2.44 Å) [34].

III. ELECTRONIC AND MAGNETIC PROPERTIES

In this section we discuss the electronic and magnetic properties of stable and metastable $(X_2O_3)_1/(Al_2O_3)_5(0001)$ superlattices with AFM and FM order. Among the $3d$ series we have identified four cases, $X =$ Ti, Mn, Co, Ni, with common features whose band structures and spin densities are shown in Fig. 2. The remaining systems are discussed towards the end of this section (see Fig. 3). The four above-mentioned cases exhibit an AFM insulating ground state. In the ferromagnetic cases with constrained symmetry of the two sublattices, we identify a common band structure with a characteristic set of four bands around E_F. Two of these bands are flat and nearly dispersionless, while the other two show a Dirac-like crossing at K close to E_F. This set of four bands bears similarities to the perovskite analogs $(LaXO_3)_2/(LaAlO_3)_4(111)$, with $X =$ Mn, Co, Ni, and originates from the single occupation

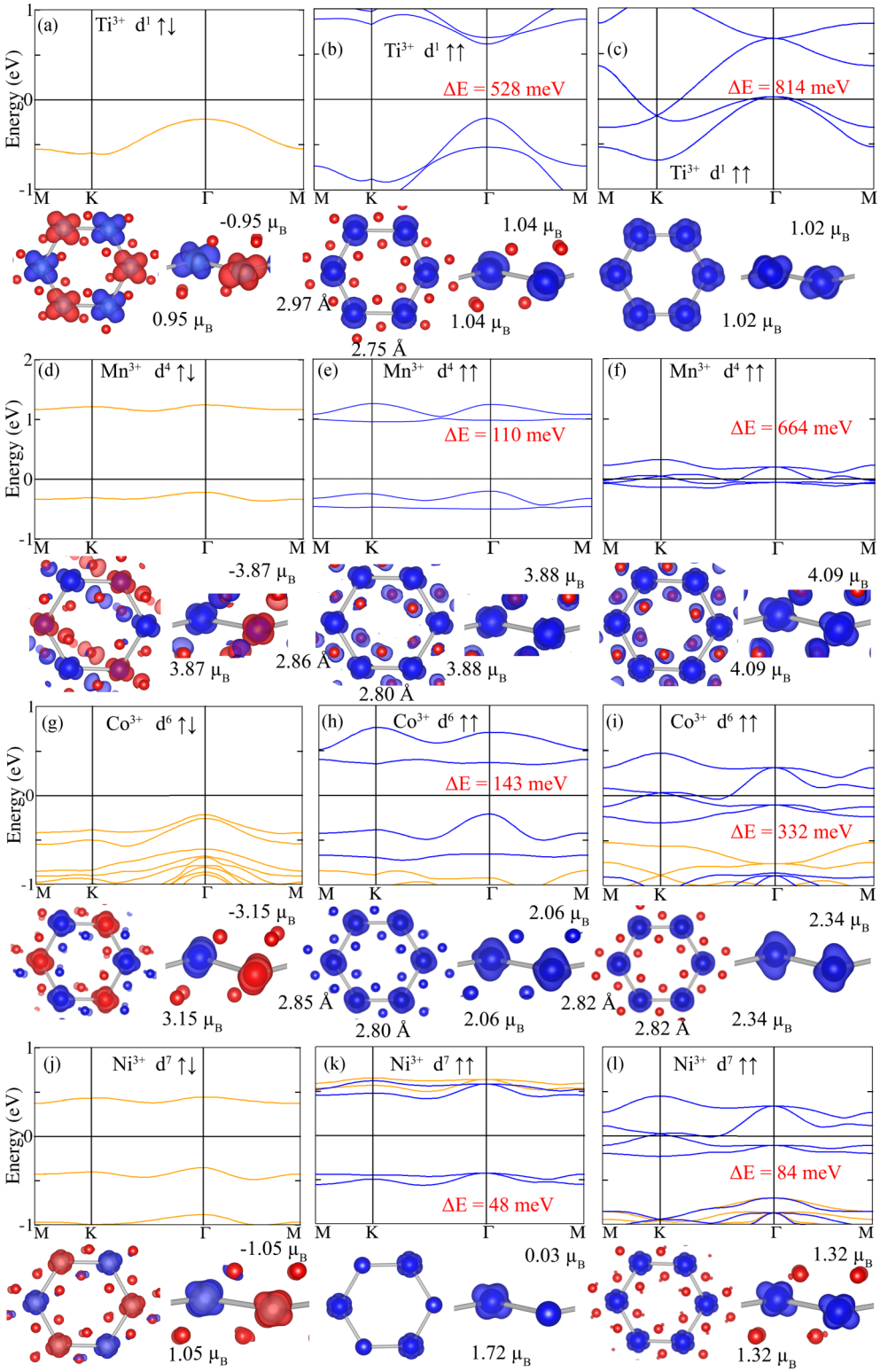

FIG. 2. Band structures and spin-density distributions of $(X_2O_3)_1/(Al_2O_3)_5(0001)$, with X = Ti, Mn, Co, Ni, for FM and AFM coupling. The spin density is integrated in the energy range from −8 eV to E_F, except in (d)–(f) and (j), where the integration interval is −0.6 eV to E_F. In the band structure blue (orange) denotes majority (minority) bands, and the Fermi level is set to zero. In the isosurfaces of the spin density blue (red) shows the majority (minority) contributions. The energy differences between the metastable and ground states are given in red; also the magnitude of the spin moments of the X ions are displayed in the spin densities.

of the e_g' and e_g manifolds, respectively, as will be discussed below. Distinct to the perovskite case, however, the Dirac crossing is not exactly at E_F, but ∼200 meV below (Ti) or slightly above (Mn, Co, and Ni) the Fermi level. The resulting electron (hole) pockets are compensated by hole (electron) pockets around Γ (Ti) or along K-Γ and Γ-M

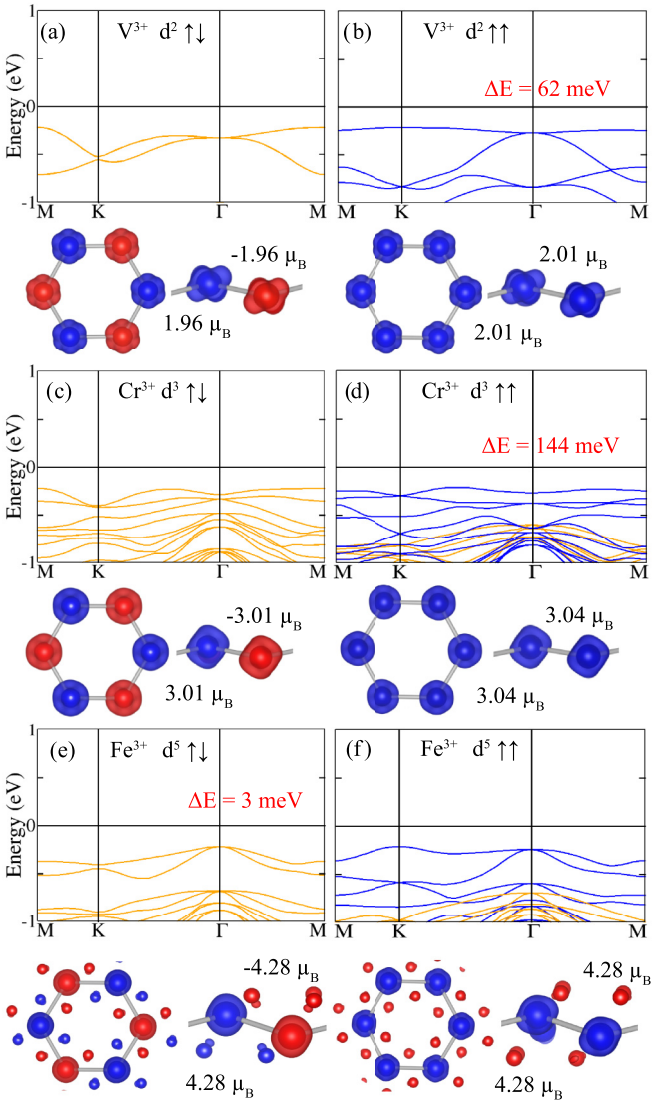

FIG. 3. Band structures and spin-density distributions integrated in the energy range from −8 eV and E_F for X = V, Cr and from −0.6 eV to E_F for Fe with FM and AFM coupling. The same color coding as in Fig. 2 is used.

for the remaining cases. In Sec. IV we will explore whether these coupled electron-hole pockets can be quenched and the Dirac point shifted to the Fermi level using epitaxial strain. A further notable feature is the variation of bandwidth of those bands: while for Ti the bandwidth is substantial [∼ 2 eV; see Fig. 2(c)], for X = Mn, Co, Ni it is much narrower [0.5–0.8 eV; see Figs. 2(f), 2(i) and 2(l)]. In all four FM cases symmetry-breaking stabilizes insulating states with significant band gaps [Figs. 2(b), 2(e), 2(h), and 2(k)]. Moreover, for both FM and AFM order we observe a rich variety of orbital reconstructions visible from the spin density of the relevant bands that are distinct from the bulk, which we discuss in more detail in the following.

In the corundum structure the symmetry of the XO_6 octahedron is reduced from octahedral to trigonal, which splits the t_{2g} orbitals into a_{1g} and e'_g. Similar to the perovskite analog $LaTiO_3$ [34], the Ti_2O_3 honeycomb layer reveals a competition between the cubic t_{2g} orbitals (d_{xy}, d_{xz}, d_{yz}) and the above-mentioned trigonal ones. In particular, a d_{xy}-shaped orbital is stabilized in the AFM ground state [Fig. 2(a)], while the symmetry-broken FM state exhibits a linear combination of two orbitals [e.g., $d_{yz}+d_{xz}$; see Fig. 2(b)]. On the other hand, the FM case with constrained symmetry of the sublattices has an e'_g orbital polarization [Fig. 2(c)]. For comparison, in the perovskite $LaTiO_3$ bilayer the FM ground state comprises a staggered order of cubic orbitals (d_{xz}, d_{yz}) [34], whereas in the corundum case the same orbital polarization occurs on both sublattices, likely related to the different (edge vs corner) connectivity in the corundum-derived honeycomb layer. It is noteworthy that these orbital polarizations are at variance with the a_{1g} occupation in bulk Ti_2O_3 [37]. As a result of the symmetry-breaking and orbital order a gap opens for the AFM ground state (2.33 eV) and the FM state (0.81 eV), which lies 528 meV higher in energy. In contrast, the FM state with symmetric sublattices is 814 meV less stable owing to the different orbital polarization (single electron in the doubly degenerate e'_g orbitals) and the resulting metallic phase with the above-described set of four majority-spin bands. It would be interesting to explore these states further, e.g., with DFT + DMFT.

The AFM ground state of X = Mn (d^4) is insulating with a gap of 1.35 eV that separates very flat bands [see Fig. 2(d)]. Its origin is a Jahn-Teller (JT) distortion which lifts the degeneracy of the singly occupied e_g band and reduces the symmetry to P1. Due to the superposition of trigonal and JT distortion the relaxation pattern is more complex, the Mn-O distances change from 1.98 and 2.10 Å (symmetric FM case) to apical distances of 2.21 and 2.09 Å and basal ones varying between 1.92 and 2.03 Å for the JT distorted case. The spin density integrated between –0.6 eV and E_F indicates a d_{z^2}-shaped orbital polarization and a strong hybridization with O2p states. We note that the orbitals on both sublattices have the same orientation, in contrast to the perovskite JT distorted $(LaMnO_3)_2/(LaAlO_3)_4(111)$ case, which shows alternating orientation of the d_{z^2}-shaped orbitals on the two sublattices [34]. Starting from the FM solution with symmetric sublattices [Fig. 2(f)], which is 0.66 eV/u.c. (unit cell) higher in energy, an orbital polarization similar to that in the AFM case arises that opens a gap of 1.20 eV in the initially metallic set of four bands [Fig. 2(e)]. This case lies 110 meV higher in energy than the AFM ground state.

X = Co and Ni also show a number of intriguing stable and metastable states. While bulk Co_2O_3 is an insulator with Co^{3+} (d^6) in a low-spin state ($S = 0$) [37], the ground state of the confined honeycomb corundum-derived lattice is an antiferromagnetic insulator with a band gap of 1.61 eV and Co in the high-spin state [calculated magnetic moment of $3.15\mu_B$; Fig. 2(g)] with a full d band in one spin direction and a single electron in the other. For ferromagnetic coupling two metastable states arise: With imposed symmetry of the two sublattices in the honeycomb layer the previously observed set of four bands emerges [Fig. 2(i)]. This state is 332 meV less stable than the ground state. When the symmetry constraint is lifted, a band gap opens that separates the two occupied from the two empty bands [143 meV above the ground state, see Fig. 2(h)]. Remarkably, the symmetry-breaking mechanism here is a dimerization of the Co sites, manifested in alternating Co-Co distances of 2.80 and 2.85 Å, in contrast to the value

of 2.82 Å in the symmetric case [note also the alternating X-X distances for X = Ti and Mn in Figs. 2(b) and 2(e), respectively].

The ground state of $(Ni_2O_3)_1/(Al_2O_3)_5(0001)$ is also an AFM insulator with a band gap of ∼0.69 eV, which separates two nearly flat bands [see Fig. 2(j)]. If for FM coupling the symmetry of the two sublattices is constrained, a metastable state occurs 84 meV above the ground state with the familiar set of four bands and a Ni magnetic moment of $1.32\mu_B$ [see Fig. 2(l)], similar to the perovskite-derived $LaNiO_3$ bilayer [24,25,32]. Releasing the symmetry constraint results in a ferromagnetic insulating state with a gap of ∼1.0 eV which arises due to disproportionation of the two Ni sublattices, reflected in a large magnetic moment of $1.72\mu_B$ on one site and a nearly quenched one on the second, $0.03\mu_B$ [see Fig. 2(k)]. This is accompanied by a bond disproportionation with Ni-O bond lengths of 2.05 and 1.97 Å at the first site and 1.91 and 1.92 Å at the second site. The corresponding NiO_6 volumes are 10.6 and 9.2 $Å^3$, respectively. This behavior bears analogies to the site disproportionation in rare-earth nickelates [63,64] and $LaNiO_3/LaAlO_3$(001) and (111) SLs [5–7,32].

The band structures and spin densities for the remaining X = V, Cr, Fe with FM and AFM coupling are shown in Fig. 3. For X = V (d^2), the e'_g doublet is fully occupied, and both the AFM and FM cases are insulating with broad band gaps (e.g., 2.70 eV for AFM). For FM alignment, the set of four bands that is half occupied for Ti is fully occupied and below E_F [see Fig. 3(b)]. Both V and Cr (d^3 with a half-filled t_{2g} subset) are trivial AFM insulators [see Figs. 3(a) and 3(c)]. In both cases the band gaps are significantly increased compared to the bulk cases due to confinement (see Tables I and II in the Supplemental Material [37]).

Interestingly, X = Fe (d^5) shows almost degenerate FM and AFM states with a slight preference for FM coupling by 3 meV/u.c., indicating weak exchange interaction. This is consistent with bulk α-Fe_2O_3, which has small AFM in-plane magnetic interaction parameters (note that the strongest AFM coupling in bulk α-Fe_2O_3 occurs to the next layer [65,66], which is quenched in the SL due to the presence of Al ions). For the FM case of X = Fe the set of four bands is fully occupied and lies 0.2 eV below E_F [Fig. 3(f)].

IV. EFFECT OF STRAIN

As discussed above, in the symmetric ferromagnetic phases of X = Ti, Mn, Co, and Ni a set four bands with a linear crossing at K is observed. However, this Dirac-like crossing is either slightly below (Ti) or slightly above (Mn, Co, Ni) the Fermi level when the system is strained at the lateral lattice constant of Al_2O_3. In this section we explore if it is possible to tune the position of the Dirac point (DP) to the Fermi level using strain. The energy vs lateral lattice constant and the band structure at the optimum lattice parameter are plotted in Figs. 4 and 5. For X = Ti the compensation of the electron and hole pockets at K and Γ is only partially possible, as at a = 5.11 Å a sharp transition from e'_g to a_{1g} orbital polarizations takes place. The band structures and electron density distributions of the bands between −1 eV and E_F just prior to and after the transition are shown in Fig. 4.

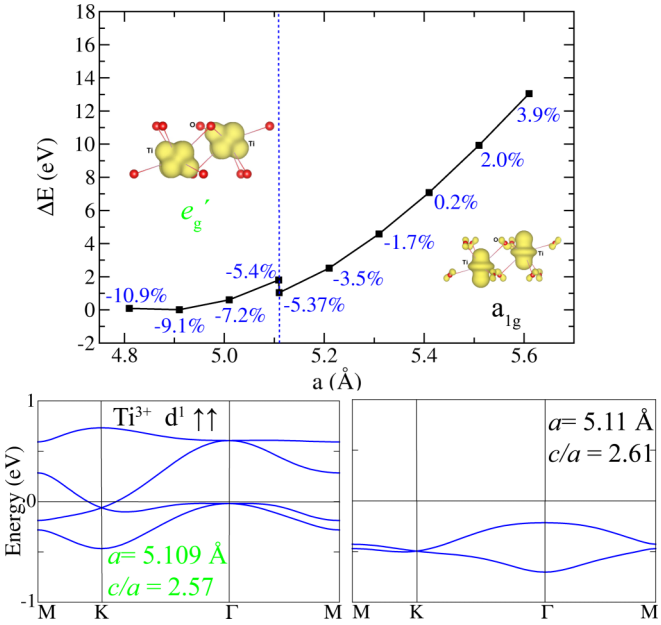

FIG. 4. Energy difference per u.c. with respect to the symmetric FM state at $a_{Al_2O_3}$. For each value of the lateral strain, the out-of-plane lattice constant was optimized within GGA+U. Additionally, the band structure is shown prior to and after the switching of orbital polarization from e'_g to a_{1g} at a = 5.11 Å.

The stability of the FM and AFM phases of X = Mn as a function of strain is displayed in Fig 5(a). While the AFM phase corresponds to the ground state for compressive strain, the energy difference to the FM state is reduced with increasing tensile strain. Moreover, a complete compensation of the electron and hole pockets can be achieved for the FM state under tensile strain for a = 5.31 Å [Fig. 5(b)]. For the metastable Co bilayer this state is reached at a smaller lateral lattice parameter, a = 5.08 Å [Fig. 5(d)]. Finally, for

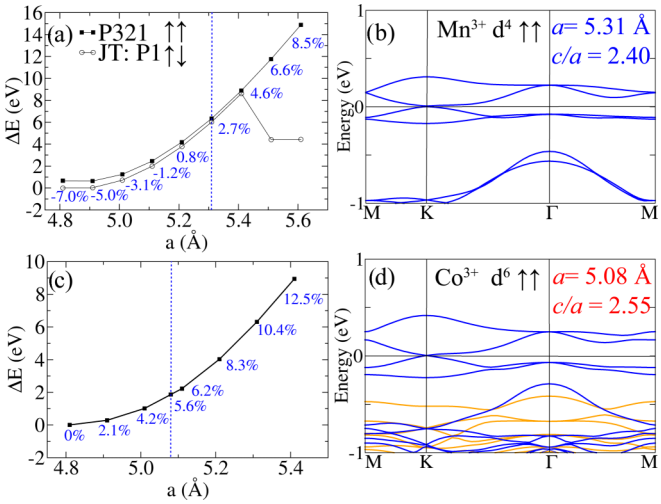

FIG. 5. Energy difference per u.c. with respect to (a) the AFM ground state of X = Mn or (c) the symmetric FM state at $a_{Al_2O_3}$ for X = Co. For each value of the lateral strain, the out-of-plane lattice constant was optimized within GGA+U. (b) and (d) The respective band structures at the optimum lattice parameters with the DP tuned to E_F.

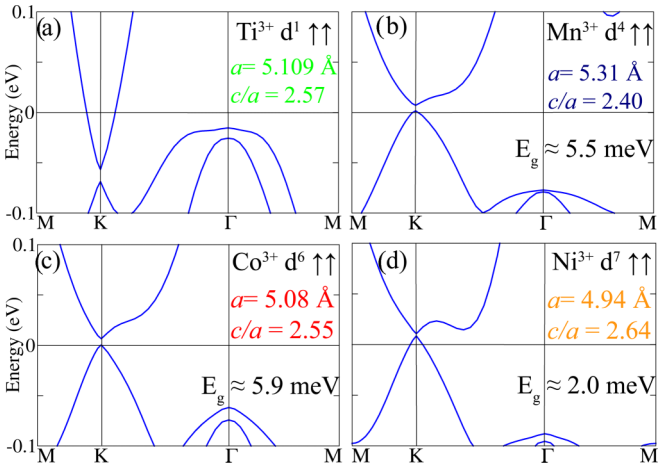

FIG. 6. GGA + U + SOC band structures for $(X_2O_3)_1/(Al_2O_3)_5(0001)$ with X = Ti, Mn, Co, Ni at the optimum lateral lattice constant and with magnetization along the [0001] direction. SOC opens a small gap at the DP at K. With the exception of X = Ti and Ni, the E_F is found to be located within the gap, resulting in a topologically nontrivial gapped state.

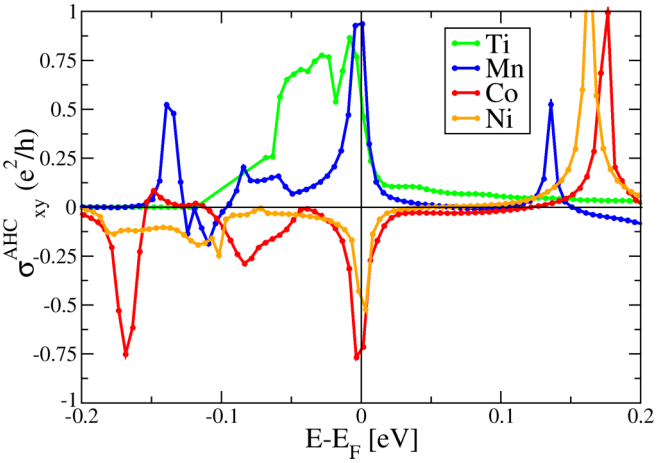

FIG. 7. AHC σ_{xy} in units of e^2/h as a function of the chemical potential for the corundum bilayers $(X_2O_3)_1/(Al_2O_3)_5(0001)$ (X = Ti, Mn, Co, Ni).

X = Ni this state occurs for a lateral lattice constant of $a = 4.94$ Å just slightly above $a_{Al_2O_3}$ (not shown here). Overall, in the latter three cases the DP can be readily tuned to the Fermi level by tensile strain, whereas the optimum lateral lattice parameter decreases with increasing band filling. We note that due to the well-known overestimation of lattice constants within GGA+U the actual transitions may occur at smaller lattice constants.

V. EFFECT OF SPIN-ORBIT COUPLING AND ANOMALOUS HALL CONDUCTIVITY

The band structures of the ferromagnetic cases of X = Ti, Mn, Co, and Ni with symmetric sublattices indicate a possible topologically nontrivial character which we analyze in the following. In the first step we explore the effect of spin-orbit coupling for the optimum lateral lattice constants obtained in the previous section, and the resulting band structures are displayed in Fig. 6. SOC leads to a gap opening at the former DP of a few meV (∼2.0–5.9 meV for the Mn and Co corundum bilayers); for Ti and Ni the avoided crossing is 50 meV below and 6 meV above E_F, respectively. We note that here the effect of SOC appears to be much smaller than for the (111)-oriented $(LaXO_3)_2/(LaAlO_3)_4(111)$, where SOC opens a gap of ∼150 meV for $LaMnO_3$ [34]. Likewise, the orbital moments are also small and range from $0.01\mu_B$ (Mn) to $0.03\mu_B$ (Ti) and $0.04\mu_B$ (Co and Ni).

For the analysis of the topological properties we project the bands around E_F to Wannier functions (WFs) using the WANNIER90 code [43]. To achieve a better localization of the WFs, we have chosen a larger energy window for the Wannier interpolation that includes, besides X $3d$ states, O $2p$ states. The Berry curvature $\Omega(k)$ is calculated through summation over all occupied bands below the Fermi level [67]:

$$\Omega(k) = -\sum_{n<E_F}\sum_{m\neq n} 2\mathrm{Im}\frac{\langle\Psi_{nk}|v_x|\Psi_{mk}\rangle\langle\Psi_{mk}|v_y|\Psi_{nk}\rangle}{(\epsilon_{mk}-\epsilon_{nk})^2}, \quad (1)$$

where Ψ_{nk} represents the spinor Bloch wave function of band n with an eigenenergy ϵ_{nk} and v_x and v_y are the components of the anomalous velocity. The AHC is computed by integrating the Berry curvature $\Omega(k)$, weighted by an occupation factor $f_n(k)$, over the Brillouin zone using a dense k-point grid of $300 \times 300 \times 50$:

$$\sigma_{xy} = -\frac{e^2}{2\pi h}\sum_n \int_{BZ} dk f_n(k)\Omega_{n,z}(k). \quad (2)$$

The anomalous Hall conductivity σ_{xy} of the corundum bilayers with the chemical potential varying ±0.2 eV around E_F is displayed in Fig. 7. All four systems show significant values approaching +1 (Ti and Mn) or −1 (Co and Ni). In particular, $(Mn_2O_3)_1/(Al_2O_3)_5(0001)$ and $(Co_2O_3)_1/(Al_2O_3)_5(0001)$ exhibit values of ∼0.94 and ∼ − 0.78 e^2/h, respectively. In contrast to other systems, like TiO_2/VO_2 [19], the plateaus here are very narrow, of the order of the small band gap opened by SOC. Hence, a small denominator and large velocity matrix elements in Eq. (1) give rise to large contributions to the Berry curvature $\Omega(k)$, as shown in Fig. 8, where sharp peaks arise around K with positive and negative values of 3000 and –8000 bohrs^2 for $(Mn_2O_3)_1/(Al_2O_3)_5(0001)$ and $(Co_2O_3)_1/(Al_2O_3)_5(0001)$, respectively. The sign of the Berry curvature correlates with the sign of the Hall conductivity.

Besides the cases presented above, we have also investigated the effect of SOC for X = Ti at the lateral lattice constant of Al_2O_3. In particular, we performed two sets of calculations: one where SOC was included after the converged GGA+U calculations and one where SOC was switched on from the start. The band structure from the first set of calculations is similar to the one displayed in Fig. 6(a) with degenerate solutions for in- and out-of-plane magnetization. In contrast, with the second approach we obtained a particularly strong effect of SOC on the total energy and band structure, although the structural differences are very small (a slight change in the degree of buckling of the honeycomb layer by 0.03 Å). For the Ti_2O_3 layer the state shown in Fig. 9(a) with magnetization along (0001) is 0.76 eV per u.c. lower in energy than the one when SOC is included on top of the converged GGA+U

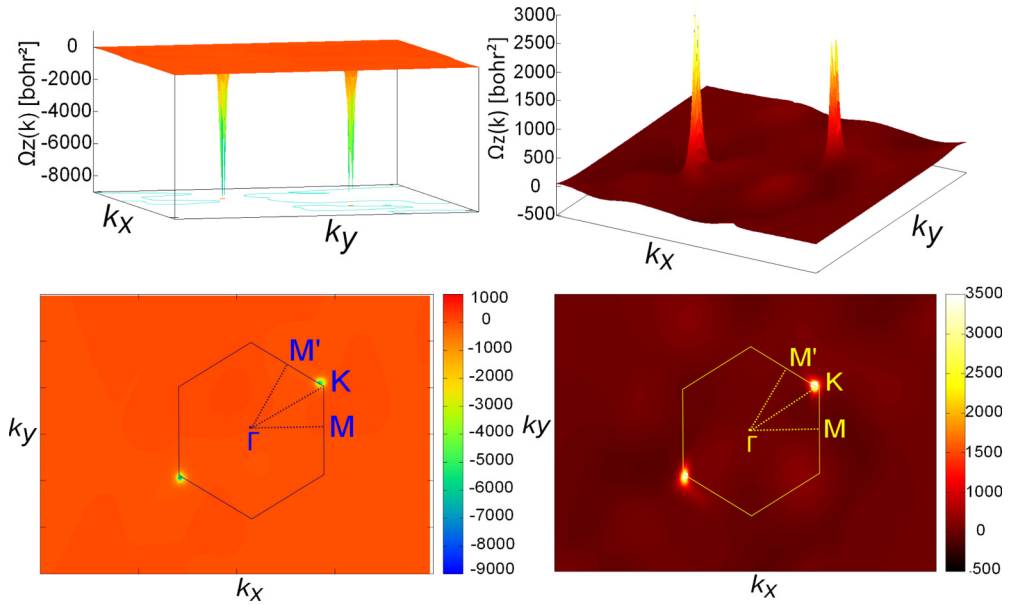

FIG. 8. Side and top views of the Berry curvature distribution $\Omega_z(k_x,k_y)$ for $(Co_2O_3)_1/(Al_2O_3)_5(0001)$ (left) and $(Mn_2O_3)_1/(Al_2O_3)_5(0001)$ (right). Note the opposite signs of $\Omega_z(k_x,k_y)$ for the two cases.

calculation, indicating strong magnetocrystalline anisotropy. The band structure is significantly modified with the initial set of four bands now split into two occupied and two empty narrow bands separated by a gap of 1.7 eV. Moreover, a large orbital moment of $-0.88\mu_B$ arises, antialigned and almost compensating the spin moment of $1.01\mu_B$. This case bears analogies to $BaFe_2(PO_4)_2$ (BFPO), for which a similarly large orbital moment of $0.7\mu_B$ was recently reported for Fe^{2+} ($S = 2$) [68]. In this compound Fe^{2+} is also arranged in a honeycomb pattern and has a d^6 occupation with completely filled inert spin-up bands and a single electron in the spin-down channel, similar to our case with Ti^{3+} ($3d^1$). As shown already in Fig. 2(c), the single electron occupies the degenerate e'_g orbitals, defined as $|e'_g\pm\rangle = \frac{1}{\sqrt{3}}(|d_{xy}\rangle + e^{\pm i\theta}|d_{yz}\rangle + e^{\mp i\theta}|d_{xz}\rangle)$, with $\theta = \frac{2\pi}{\sqrt{3}}$, whereas the a_{1g} orbital is higher in energy. As discussed recently by Kim and Kee for BFPO [69], SOC acts as an atomic orbital Zeeman term: The solution with $L_z = 1$ and magnetization along the [0001] direction breaks the degeneracy of the e'_g orbitals, causing a transfer of charge from the e'_g+ to the e'_g- orbital and thereby opening a significant gap as in BFPO [68]. Due to the antiparallel alignment of the spin and orbital moment the total moment is almost quenched, and $(Ti_2O_3)_1/(Al_2O_3)_5(0001)$ can be regarded as a possible realization of Haldane's model of spinless fermions hopping on a honeycomb lattice [9]. The advantage compared to BFPO is that there are no further d electrons, e.g., in the other spin channel, to interfere with this state. Because the strong SOC effect occurs only for FM coupling, the energy difference between the AFM and FM decreases by an order of magnitude from 814 meV/u.c. (GGA+U) to 56 meV/u.c. (GGA+U+SOC), making this intriguing state more likely to be realized. Moreover, a calculation of Γ-phonon modes indicates an unusual case where strong SOC dynamically stabilizes the system (for more details see the Supplemental Material [37]).

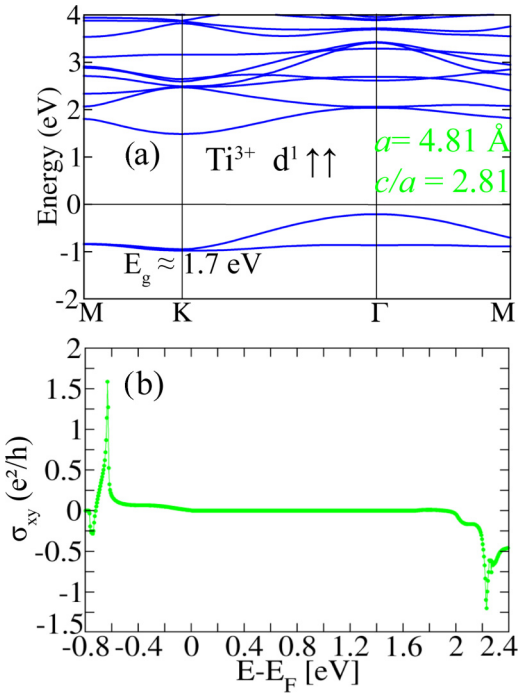

FIG. 9. Strong effect of SOC for $(Ti_2O_3)_1/(Al_2O_3)_5(0001)$ at $a_{Al_2O_3}$: (a) band structure and (b) AHC plotted vs the chemical potential.

A further analogy to BFPO [69] appears when analyzing the band structure and QAH conductivity in Figs. 9(a) and 9(b): although $\sigma_{xy} = 0$ at E_F points to a trivial FM Mott insulator, positive (negative) spikes at -0.8 and 2.2 eV indicate an occupied (empty) pair of nontrivial bands with opposite Chern numbers and chirality. For BFPO Kim and Kee [69] proposed substitution of Ba^{2+} by mono- or trivalent cations in order to shift E_F between the lower and upper pairs of Chern bands and thereby design a QAHI. This scenario is more difficult to realize for the corundum case since cations other than trivalent

are less common in this structure, but it needs to be explored in further studies.

VI. SUMMARY

In summary, our DFT+U results on $(X_2O_3)_1/(Al_2O_3)_5(0001)$ indicate a broad variety of electronic phases with respect to orbital polarization and spin state, induced by the confinement of the $3d$ honeycomb layer, that are not available in the bulk X_2O_3 compounds. While the ground states in most cases are trivial AFM Mott insulators, followed in stability by symmetry-broken ferromagnetic insulating states, for X = Ti, Mn, Co, and Ni with ferromagnetic coupling and imposed symmetry of the two sublattices, a characteristic set of four bands with two being relatively flat and two crossing at K close to the Fermi level emerges. This feature is similar to the one obtained for X = Mn, Co [34], and Ni [24,25,32,34] in the perovskite $(LaXO_3)_2/(LaAlO_3)_4(111)$ superlattices and is a result of the single occupation of the degenerate e_g' or e_g states, respectively. Further analogies arise to the nonmagnetic d^8 configuration in $5d$ corundum-derived honeycomb lattices (i.e., d^4, single occupation of e_g states in each spin channel). Still, the latter topologically nontrivial configuration is metastable (the ground state is found to be AFM for $U > -3$ eV) and transforms into a trivial one with increasing U or tensile strain [36]. Further studies are necessary to address the effect of time-reversal symmetry breaking in $4d$ and $5d$ systems.

For $(X_2O_3)_1/(Al_2O_3)_5(0001)$ with X = Mn, Co, and Ni and symmetric sublattices, the above-mentioned Dirac crossing can be tuned to the Fermi level using strain, while for Ti this is hampered by a switching of the orbital polarization from e_g' to a_{1g}. SOC opens a small gap of several meV in these band structures and leads to a notable anomalous Hall conductivity at the Fermi level, arising from the sharp peak of the Berry curvature at the avoided band crossing at K. Overall, the tendency towards topological phases is weaker, and the gap sizes are smaller than in the perovskite bilayers. For comparison, in the $LaMnO_3$ perovskite SL a significant gap of 150 meV is opened by SOC, leading to a metastable Chern insulator [34].

Finally, for $(Ti_2O_3)_1/(Al_2O_3)_5(0001)$ we obtain a case of particularly strong SOC at $a_{Al_2O_3}$ that opens a large trivial Mott insulating gap (1.7 eV) with an extremely high orbital moment ($-0.88\mu_B$) which almost compensates the spin moment of $1.01\mu_B$, thus making the system a promising candidate for the realization of Haldane's model of spinless fermions on a honeycomb lattice. We note also the presence of nontrivial pairs of bands below and above E_F, suggesting that a Chern insulator may be accessible through suitable electron/hole doping. This strong SOC effect stabilizes the system dynamically and significantly reduces the energy difference to the AFM ground state from 814 meV without SOC to 56 meV.

The epitaxial growth of corundum films and heterostructures has been less in the focus of investigation compared to perovskites but offers the advantage that fewer elements are involved (e.g., only X and Al ions, instead of three or four different cations in a perovskite superlattice). Several studies have reported the successful growth of corundum thin films on $Al_2O_3(0001)$ using molecular beam epitaxy [70–72], pulsed laser deposition [73], a helicon plasma [74], and rf magnetron sputtering [75]. These reports suggest that the growth of corundum-based superlattices is viable, and we trust that the electronic phases predicted here will inspire new experimental studies for their realization.

ACKNOWLEDGMENTS

We acknowledge useful discussions with W. E. Pickett and V. Pardo on honeycomb lattices and M. E. Gruner on phonon calculations and support by the German Science Foundation (Deutsche Forschungsgemeinschaft, DFG) within the SFB/TRR 80, project G3, and computational time at the Leibniz-Rechenzentrum Garching within project pr87ro.

[1] H. Y. Hwang, Y. Iwasa, M. Kawasaki, B. Keimer, N. Nagaosa, and Y. Tokura, Nat. Mater. **11**, 103 (2012).
[2] J. Mannhart and D. G. Schlom, Science **327**, 1607 (2010).
[3] J. Chakhalian, A. J. Millis, and J. Rondinelli, Nat. Mater. **11**, 92 (2012).
[4] M. Lorenz, M. S. R. Rao, T. Venkatesan, E. Fortunato, P. Barquinha, R. Branquinho, D. Salgueiro, R. Martins, E. Carlos, A. Liu, F. K. Shan, M. Grundmann, H. Boschker, J. Mukherjee, M. Priyadarshini, N. DasGupta, D. J. Rogers, F. H. Teherani, E. V. Sandana, P. Bove, K. Rietwyk, A. Zaban, A. Veziridis, A. Weidenkaff, M. Muralidhar, M. Murakami, S. Abel, J. Fompeyrine, J. Zuniga-Perez, R. Ramesh, N. A. Spaldin, S. Ostanin, V. Borisov, I. Mertig, V. Lazenka, G. Srinivasan, W. Prellier1, M. Uchida, M. Kawasaki, R. Pentcheva, P. Gegenwart, F. Miletto Granozio, J. Fontcuberta, and N. Pryds, J. Phys. D **49**, 433001 (2016).
[5] A. V. Boris, Y. Matiks, E. Benckiser, A. Frano, P. Popovich, V. Hinkov, P. Wochner, M. Castro-Colin, E. Detemple, V. K. Malik, C. Bernhard, T. Prokscha, A. Suter, Z. Salman, E. Morenzoni, G. Cristiani, H.-U. Habermeier, and B. Keimer, Science **332**, 937 (2011).
[6] J. W. Freeland, J. Liu, M. Kareev, B. Gray, J. W. Kim, P. Ryan, R. Pentcheva, and J. Chakhalian, Europhys. Lett. **96**, 57004 (2011).
[7] A. Blanca-Romero and R. Pentcheva, Phys. Rev. B **84**, 195450 (2011).
[8] D. Xiao, W. Zhu, Y. Ran, N. Nagaosa, and S. Okamoto, Nat. Commun. **2**, 596 (2011).
[9] F. D. M. Haldane, Phys. Rev. Lett. **61**, 2015 (1988).
[10] H. Weng, R. Yu, X. Hu, X. Dai, and Z. Fang, Adv. Phys. **64**, 227 (2015).
[11] Y. Ren, Z. Qiao, and Q. Niu, Rep. Progr. Phys. **79**, 066501 (2016).
[12] C.-X. Liu, X.-L. Qi, X. Dai, Z. Fang, and S.-C. Zhang, Phys. Rev. Lett. **101**, 146802 (2008).
[13] R. Yu, W. Zhang, H.-J. Zhang, S.-C. Zhang, X. Dai, and Z. Fang, Science **329**, 61 (2010).
[14] C. Fang, M. J. Gilbert, and B. A. Bernevig, Phys. Rev. Lett. **112**, 046801 (2014).
[15] H. Zhang, C. Lazo, S. Blügel, S. Heinze, and Y. Mokrousov, Phys. Rev. Lett. **108**, 056802 (2012).
[16] M. Zhou, Z. Liu, W. Ming, Z. Wang, and F. Liu, Phys. Rev. Lett. **113**, 236802 (2014).

[17] H. Zhang, J. Wang, G. Xu, Y. Xu, and S.-C. Zhang, Phys. Rev. Lett. **112**, 096804 (2014).

[18] K. F. Garrity and D. Vanderbilt, Phys. Rev. B **90**, 121103(R) (2014).

[19] H. Huang, Z. Liu, H. Zhang, W. Duan, and D. Vanderbilt, Phys. Rev. B **92**, 161115(R) (2015).

[20] T. Cai, X. Li, F. Wang, S. Ju, J. Feng, and C.-D. Gong, Nano Lett. **15**, 6434 (2015).

[21] J. L. Lado, D. Guterding, P. Barone, R. Valenti, and V. Pardo, Phys. Rev. B **94**, 235111 (2016).

[22] A. M. Cook and A. Paramekanti, Phys. Rev. Lett. **113**, 077203 (2014).

[23] S. Baidya, U. V. Waghmare, A. Paramekanti, and T. Saha-Dasgupta, Phys. Rev. B **94**, 155405 (2016).

[24] K.-Y. Yang, W. Zhu, D. Xiao, S. Okamoto, Z. Wang, and Y. Ran, Phys. Rev. B **84**, 201104(R) (2011).

[25] A. Rüegg and G. A. Fiete, Phys. Rev. B **84**, 201103 (2011).

[26] A. Rüegg, C. Mitra, A. A. Demkov, and G. A. Fiete, Phys. Rev. B **85**, 245131 (2012); **88**, 115146 (2013).

[27] S. Middey, D. Meyers, M. Kareev, E. J. Moon, B. A. Gray, X. Liu, J. W. Freeland, and J. Chakhalian, Appl. Phys. Lett. **101**, 261602 (2012).

[28] J. L. Lado, V. Pardo, and D. Baldomir, Phys. Rev. B **88**, 155119 (2013).

[29] S. Okamoto, Phys. Rev. Lett. **110**, 066403 (2013).

[30] D. Doennig, W. E. Pickett, and R. Pentcheva, Phys. Rev. Lett. **111**, 126804 (2013).

[31] S. Okamoto, W. Zhu, Y. Nomura, R. Arita, D. Xiao, and N. Nagaosa, Phys. Rev. B **89**, 195121 (2014).

[32] D. Doennig, W. E. Pickett, and R. Pentcheva, Phys. Rev. B **89**, 121110 (2014).

[33] S. Middey, D. Meyers, D. Doennig, M. Kareev, X. Liu, Y. Cao, Z. Yang, J. Shi, L. Gu, P. J. Ryan, R. Pentcheva, J. W. Freeland, and J. Chakhalian, Phys. Rev. Lett. **116**, 056801 (2016).

[34] D. Doennig, S. Baidya, W. E. Pickett, and R. Pentcheva, Phys. Rev. B **93**, 165145 (2016).

[35] H. Guo, S. Gangopadhyay, O. Köksal, R. Pentcheva, and W. E. Pickett, npj Quantum Mater. **2**, 4 (2017).

[36] J. F. Afonso and V. Pardo, Phys. Rev. B **92**, 235102 (2015).

[37] See Supplemental Material at http://link.aps.org/supplemental/10.1103/PhysRevB.97.035126 for details on the X_2O_3 bulk and superlattices and dependence on U. Comparison to previous experimental and theoretical results on the bulk compounds is also provided in Refs. [46–62].

[38] G. Kresse and J. Furthmüller, Phys. Rev. B **54**, 11169 (1996).

[39] G. Kresse and D. Joubert, Phys. Rev. B **59**, 1758 (1999).

[40] J. P. Perdew, K. Burke, and M. Ernzerhof, Phys. Rev. Lett. **77**, 3865 (1996).

[41] S. L. Dudarev, G. A. Botton, S. Y. Savrasov, C. J. Humphreys, and A. P. Sutton, Phys. Rev. B **57**, 1505 (1998).

[42] K. Schwarz and P. Blaha, Comput. Mater. Sci. **28**, 259 (2003).

[43] A. A. Mostofi, J. R. Yates, Y.-S. Lee, I. Souza, D. Vanderbilt, and N. Marzari, Comput. Phys. Commun. **178**, 685 (2008).

[44] N. Marzari, A. A. Mostofi, J. R. Yates, I. Souza, and D. Vanderbilt, Rev. Mod. Phys. **84**, 1419 (2012).

[45] R. E. Newnham and Y. M. de Haan, Z. Kristallogr. **117**, 235 (1962).

[46] S. V. Ovsyannikov, A. M. Abakumov, A. A. Tsirlin, W. Schnelle, R. Egoavil, J. Verbeeck, G. Van Tendeloo, K. V. Glazyrin, M. Hanfland, and L. Dubrovinsky, Angew. Chem., Int. Ed. Engl. **52**, 1494 (2013).

[47] S. P. Tandon and J. P. Gupta, Solid State Commun. **7**, 1793 (1969).

[48] M. Catti and G. Sandrone, Faraday Discuss. **106**, 189 (1997).

[49] V. Singh and D. T. Major, Inorg. Chem. **55**, 3307 (2016).

[50] C. E. Rice and W. R. Robinson, Acta Crystallogr., Sect. B **33**, 1342 (1977).

[51] S. H. Shin, G. V. Chandrashekhar, R. E. Loehman, J. M. Honig, and R. J. Sladek, Phys. Rev. B **8**, 1364 (1973).

[52] J. M. Honig and T. B. Reed, Phys. Rev. **174**, 1020 (1968).

[53] G. A. Thomas, D. H. Rapkine, S. A. Carter, A. J. Millis, T. F. Rosenbaum, P. Metcalf, and J. M. Honig, Phys. Rev. Lett. **73**, 1529 (1994).

[54] M. M. Qazilbash, A. A. Schafgans, K. S. Burch, S. J. Yun, B. G. Chae, B. J. Kim, H. T. Kim, and D. N. Basov, Phys. Rev. B **77**, 115121 (2008).

[55] G. A. Sawatzky and D. Post, Phys. Rev. B **20**, 1546 (1979).

[56] J. A. Crawford and R. W. Vest, J. Appl. Phys. **35**, 2413 (1964).

[57] C. S. Cheng, H. Gomi, and H. Sakata, Phys. Status Solidi A **155**, 417 (1996).

[58] R. Hasimur, R. M. Laha, D. K. Maiti, and S. K. Ghosh, RSC Adv. **5**, 33923 (2015).

[59] S. Mochizuki, Phys. Status Solidi A **41**, 591 (1977).

[60] Y. Guo, S. J. Clark, and J. Robertson, J. Phys. Condens. Matter **24**, 325504 (2012).

[61] G. Kresse, S. Surnev, J. Schoiswohl, and F. P. Netzer, Surf. Sci. **555**, 118 (2004).

[62] S. Y. Ezhov, V. I. Anisimov, D. I. Khomskii, and G. A. Sawatzky, Phys. Rev. Lett. **83**, 4136 (1999).

[63] H. Park, A. J. Millis, and C. A. Marianetti, Phys. Rev. Lett. **109**, 156402 (2012).

[64] S. Johnston, A. Mukherjee, I. Elfimov, M. Berciu, and G. A. Sawatzky, Phys. Rev. Lett. **112**, 106404 (2014).

[65] H. Sadat Nabi, R. J. Harrison, and R. Pentcheva, Phys. Rev. B **81**, 214432 (2010).

[66] H. Sadat Nabi and R. Pentcheva, Phys. Rev. B **83**, 214424 (2011).

[67] X. Wang, J. R. Yates, I. Souza, and D. Vanderbilt, Phys. Rev. B **74**, 195118 (2006).

[68] Y.-J. Song, K.-W. Lee, and W. E. Pickett, Phys. Rev. B **92**, 125109 (2015).

[69] H. S. Kim and H.-Y. Kee, npj Quantum Mater. **2**, 20 (2017).

[70] S. E. Chamberlin, T. C. Kaspar, M. E. Bowden, V. Shutthanandan, B. Kabius, S. Heald, D. J. Keavney, and S. A. Chambers, J. Appl. Phys. **116**, 233702 (2014).

[71] T. C. Kaspar, S. E. Chamberlin, M. E. Bowden, R. Colby, V. Shutthanandan, S. Manandhar, Y. Wang, P. V. Sushko, and S. A. Chambers, J. Phys. Condens. Matter **26**, 135005 (2014).

[72] T. Dennenwaldt, M. Lübbe, M. Winklhofer, A. Müller, M. Döblinger, H. Sadat Nabi, M. Gandman, T. Cohen-Hyams, W. D. Kaplan, W. Moritz, R. Pentcheva, and C. Scheu, J. Mater. Sci. **50**, 122 (2015).

[73] E. Popova, B. Warot-Fonrose, H. Ndilimabaka, M. Bibes, N. Keller, B. Berini, K. Bouzehouane, and Y. Dumont, J. Appl. Phys. **103**, 093909 (2008).

[74] Y. Takada, M. Nakanishi, T. Fujiia, and J. Takada, Appl. Phys. Lett. **92**, 252102 (2008).

[75] Y. Gao, H. Leiste, M. Stueber, and S. Ulrich, J. Cryst. Growth **457**, 158 (2017).